TOI-5126: a hot super-Neptune and warm Neptune pair discovered by *TESS* and *CHEOPS*

Tyler R. Fairnington [1]⋆ Emma Nabbie,[1] Chelsea X. Huang,[1]† George Zhou,[1]‡ Orion Foo,[2]
Sarah Millholland,[2] Duncan Wright,[1] Alexandre A. Belinski,[3] Allyson Bieryla [4] David R. Ciardi,[5]
Karen A. Collins,[4] Kevin I. Collins,[6] Mark Everett,[7] Steve B. Howell,[8] Jack J. Lissauer,[8]
Michael B. Lund,[5] Felipe Murgas,[9,10] Enric Palle,[9,10] Samuel N. Quinn,[4] Howard M. Relles,[4]
Boris S. Safonov,[3] Richard P. Schwarz,[4] Nicholas J. Scott,[8] Gregor Srdoc,[11] George Ricker,[2]
Roland Vanderspek,[2] Sara Seager,[2,12,13] David W. Latham,[4] Joshua W. Winn,[14] Jon M. Jenkins,[8]
Luke G. Bouma [15] Avi Shporer,[2] Eric B. Ting,[8] Diana Dragomir [16] Michelle Kunimoto[2]
and Nora L. Eisner[15,17]

Affiliations are listed at the end of the paper

ABSTRACT

We present the confirmation of a hot super-Neptune with an exterior Neptune companion orbiting a bright (V = 10.1 mag) F-dwarf identified by the Transiting Exoplanet Survey Satellite (*TESS*). The two planets, observed in sectors 45, 46, and 48 of the *TESS* extended mission, are $4.74^{+0.16}_{-0.14}$ and $3.86^{+0.17}_{-0.16}$ $R_\oplus$ with $5.4588385^{+0.0000070}_{-0.0000072}$ and $17.8999^{+0.0018}_{-0.0013}$ d orbital periods, respectively. We also obtained precise space-based photometric follow-up of the system with ESA's CHaracterising ExOplanets Satellite to constrain the radius and ephemeris of TOI-5126 b. TOI-5126 b is located in the 'hot Neptune Desert' and is an ideal candidate for follow-up transmission spectroscopy due to its high-predicted equilibrium temperature ($T_{eq} = 1442^{+46}_{-40}$ K) implying a cloud-free atmosphere. TOI-5126 c is a warm Neptune ($T_{eq} = 971^{+31}_{-27}$ K) also suitable for follow-up. Tentative transit timing variations have also been identified in analysis, suggesting the presence of at least one additional planet, however this signal may be caused by spot-crossing events, necessitating further precise photometric follow-up to confirm these signals.

Key words: planets and satellites: detection – techniques: photometric – stars: individual TOI-5126.

1 INTRODUCTION

Super-Neptunes are a class of planets potentially bridging the gap between Neptune and Jovian planets[1] (4–8 $R_\oplus$). Despite being of similar sizes, they exhibit a significant diversity in mass, almost uniformly distributed between 6 and 135 $M_\oplus$ (Akeson et al. 2013; Petigura et al. 2017). Given the absence of such planets in the Solar system, studying the population provides extra insights on the versatility of the planet formation process around other stars.

An archetypal example of the super-Neptune class is GJ 436 b (Gillon et al. 2007). It has a Neptune-like radius coupled with a relatively high density. It also has an inferred rocky element core and substantial H/He envelope (Fortney, Marley & Barnes 2007). Its characteristics appear to deviate from the theorized $\approx 5\,M_\oplus$ threshold needed for runaway accretion (Lee & Chiang 2016a), highlighting

our lack of understanding about the formation channels from which this class originates. *Kepler* and the subsequent *K2* mission (Borucki et al. 2010; Howell et al. 2014) enabled the first population studies of these planets. Petigura et al. (2017) proposed that super-Neptunes form in gas-depleted discs (Lee, Chiang & Ormel 2014) or from planet–planet mergers (Petigura et al. 2017). Both of these formation scenarios lead to heavy elements in the planets atmosphere, making these theories testable with bright systems hosting super-Neptunes.

However, the majority of confirmed super-Neptunes discovered by the *Kepler* and *K2* missions orbit around relatively faint stars, posing challenges for detailed atmosphere characterization. The all-sky *Transiting Exoplanet Survey Satellite* (*TESS*, Ricker et al. 2015) mission aims to survey the entire sky for candidates around some of the brightest nearby stars, providing the best opportunity to further our knowledge of super-Neptunes. *TESS* has already identified several unique super-Neptunes, including LTT 9779 b (Jenkins et al. 2020a) and TOI-849 b (Armstrong et al. 2020). Both reside in the 'hot Neptune desert' (Mazeh, Holczer & Faigler 2016), creating further challenges to their formation and evolution models. Planets in this close-in highly irradiated period space are usually thought to be most susceptible to photoevaporation (Owen & Jackson 2012; Jin et al.

⋆ E-mail: tyler.fairnington@usq.edu.au
† ARC DECRA Fellow.
‡ ARC DECRA Fellow.
[1]In the literature, these planets are also often referred as Sub-Saturns.

2014; Lopez 2017) and tidal stripping (Matsakos & Königl 2016; Owen & Lai 2018). LTT 9779 b is an ideal target for follow-up atmospheric studies, with a Spitzer phase curve already suggesting a high-metallicity atmosphere (Crossfield et al. 2020). Efforts to understand this population can be most fruitful via multiplanet systems, where comparative planetology is possible.

In this paper, we present the discovery of a multi-transiting system around the F-dwarf ($T_{\rm eff}= 6150^{+130}_{-100}$ K) TOI-5126. The system, first discovered by *TESS*, hosts a hot super-Neptune located in the 'hot Neptune Desert', and an exterior warm Neptune. The brightness of TOI-5126 and the high-predicted equilibrium temperatures of planet b (1442^{+46}_{-40} K) and c (971^{+31}_{-27} K) make these planets ideal for future follow-up, including atmospheric comparative planetology studies. In Section 2, we present the photometric, imaging and spectroscopic observations that led to the discovery and confirmation of the TOI-5126 system. Section 3 discusses the derived stellar parameters of TOI-5126, as well as the global modelling and analysis of the system. The results of our analysis are presented in Section 4, including validation of TOI-5126 b and TOI-5126 c, transit timing variations (TTVs), and future follow-up opportunities.

2 OBSERVATIONS AND DATA ANALYSIS

2.1 Photometry

2.1.1 TESS

TOI-5126 (TIC 27064468) was observed by TESS nearly continuously on both the 2 min cadence target pixel stamps and the 10 min Full Frame Images (FFIs) in sectors 45 (Camera 3 CCD 4) and 46 (Camera 2 CCD 2), with an additional sector (sector 48, Camera 1 CCD 4) a month later. The observations were taken from UT 2021-Nov-06 to UT 2022-Feb-26, for a total of ≈76 d.

In sector 46, systematic errors were observed in the first 13 h of data due to a pointing adjustment.[2] To mitigate these errors, we utilized quality flags to mask out scattered light and other systematic effects in the light curves.

The light curves of TOI-5126 were processed by both the *TESS* Science Processing Operations Center (SPOC; Jenkins et al. 2016), located at NASA Ames Research Center. The SPOC conducted a transit search of Sector 45 2-min cadence data on UT 2021 January 09 with an adaptive, noise-compensating matched filter (Jenkins, Caldwell & Borucki 2002; Jenkins et al. 2010, 2020b), producing a Threshold Crossing Event for which an initial limb-darkened transit model was fitted (Li et al. 2019) and a suite of diagnostic tests were conducted to help make or break the planetary nature of the signal (Twicken et al. 2018). Transit signatures were also detected in a search of FFI 10-min cadence data by the Quick Look Pipeline (QLP) at MIT (Huang et al. 2020). The TESS Science Office reviewed the vetting information and issued an alert for TOI-5126 b on UT 2022 January 25 based and an alert for TOI-5126 c on UT 2022 February 08 (Guerrero et al. 2021) based on QLP data. The signals were repeatedly recovered as additional observations were made including in both Sectors 46 and 48, as well as SPOC multi-sector searches (42–46, 14–50). The transit signatures again passed all the diagnostic tests presented in the Data Validation reports. Specifically, difference images from the Sectors 42–46 data located the catalogue location of TOI-5126 b and TOI-5126 c within 9.0 ± 5.0 and 5.2 ± 5.8 arcsec of

the transit source. The latest SPOC results captured signals for planets b [Signal-to-Noise (SNR): 26.1; Multiple Event Statistic (MES): 19.9] and c (SNR: 10.4; MES: 9.9). The transit events of TOI-5126 b were also identified by the Planet Hunters *TESS* citizen science project (Eisner et al. 2020) and uploaded to Exoplanet Follow-up Observation Program (exoFOP) as communitiy objects of interest on UT 2022 January 12.

For our analysis, a modification of the deblended SPOC Simple Aperture Photometry (SAP) light curves (Twicken et al. 2010; Morris et al. 2020) were used in modelling (see Fig. 1). Stellar variability was accounted for by simultaneously fitting for a polynomial trend around each transit as part of our global analysis. Two transits were manually excluded due to them occurring near a data gap (see Figure 2) Our ephemeris and radius precision did not noticeably suffer from these excluded transits. The details of the global fit will be presented in Section 3.2.

2.1.2 CHEOPS

To refine the radius and ephemeris of TOI-5126 b, we obtained space-based photometric observations with *CHaracterising ExOplanets Satellite (CHEOPS)* (Benz et al. 2021). Observations were attained through the *CHEOPS* Guest Observers Programme (AO3-023). A first observation of TOI-5126 b occurred on 2022 February 16 21:44 UT for a duration of 11.72 h. The preliminary data was processed through the *CHEOPS* Data Reduction Pipeline (version 13.1; Hoyer et al. 2020) on 2023 February 17 18:46 UT. The visit consisted of seven *CHEOPS* orbits, with a four orbit pre-ingress and one orbit post-egress out-of-transit baseline. An additional visit of TOI-5126 b occurred on 2023 February 27 23:55 UT in an attempt to identify an ingress/egress with high efficiency, resulting in a longer 14.14 h observation, with two orbits pre-ingress and five orbits post-egress. We obtained a third visit of TOI-5126 b on 2023 March 27 04:44 where we successfully caught both the ingress and egress over an observation duration of 10.96 h. The full details of observations are listed in Table 1.

The raw *CHEOPS* light curves were detrended simultaneously with the transit modelling to best incorporate and propagate the uncertainties associated with the instrument into our final system parameters. Observations with poor data quality flags, and those that fail an iterative 5-σ outlier rejection, were rejected from subsequent analyses. To correct for the *CHEOPS* systematics, we followed the trend model in the PYCHEOPS package (Maxted et al. 2022). This model fits for spacecraft and environmental variations, including the roll angle, ϕ, the background flux, BG, the contamination in the aperture, CONTAM, smearing correction, SMEAR, and the x and y point spread function (PSF) centroid coordinates, DX & DY. The raw *CHEOPS* light curves were detrended by fitting a least-squares model to the light-curve residuals, which provided us with the best parameters for the trend model. These parameters were then applied to the trend function and subtracted from the raw flux to provide us with the detrended *CHEOPS* light curves, seen in Fig. 3.

2.1.3 Ground-based photometric follow-up

Due to the coarse angular resolution of both *TESS* and *CHEOPS*, eclipsing binary stars within their apertures may mimic a transit event on the target star. To confirm the on-target detection of TOI-5126, we obtained ground-based photometric observations of both planets. We used the TESS Transit Finder, which is a customized
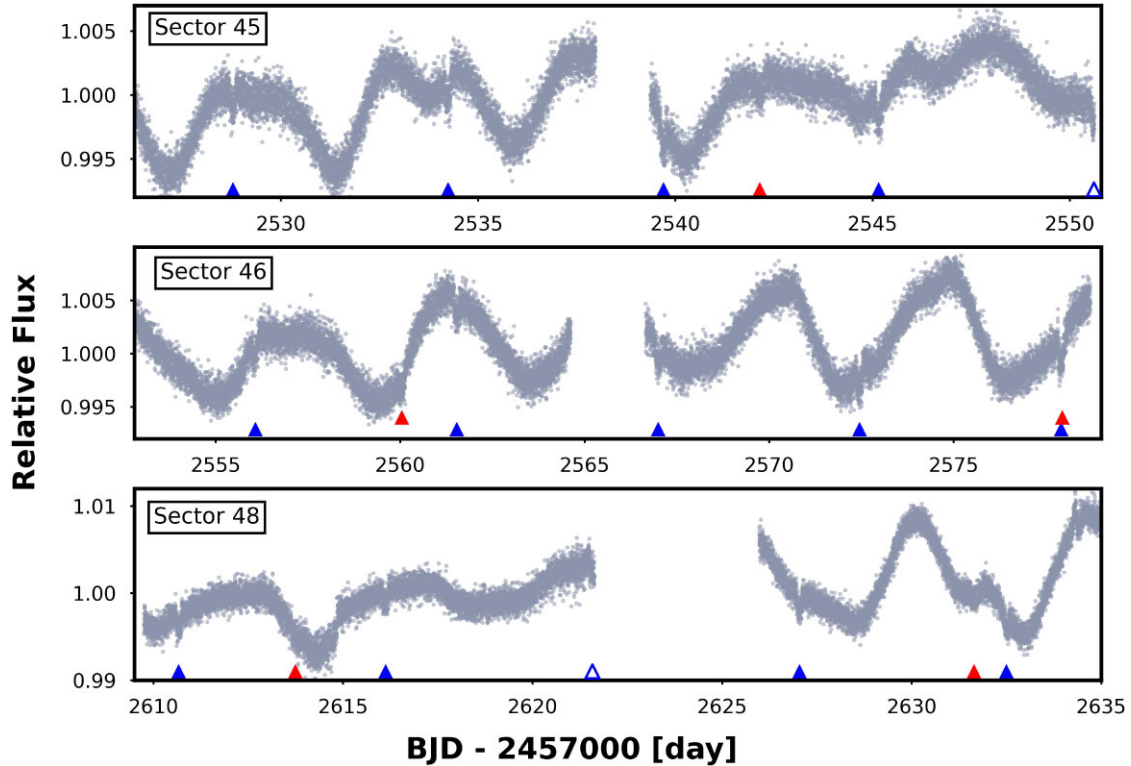

Figure 1. *TESS* SPOC SAP light curve of TOI-5126 from all observed sectors. Blue triangles mark each transit of TOI-5126 b, with red arrows for transits of TOI-5126 c. Empty triangles indicate the transits not used in global modelling.

Table 1. List of CHEOPS observations.

Planet	Start date (UT)	Duration (h)	Valid points (#)	File key	Efficiency (per cent)	Exp. time (s)
b	2023-02-16 21:44	11.72	422	CH_PR230023_TG000301_V0200	59.20	60.0
b	2023-02-27 23:55	14.14	549	CH_PR230023_TG000302_V0200	64.60	60.0
b	2023-03-27 04:44	10.96	458	CH_PR230023_TG000501_V0200	65.30	60.0

version of the TAPIR software package (Jensen 2013), to schedule our transit observations. TOI-5126 b was observed in the z_s filter by two 1.0 m Las Cumbres Observatory Global Network (LCOGT; Brown et al. 2013) telescopes simultaneously at the McDonald Observatory (McD) in Fort Davis, Texas (2022 March 10 UT). The transit event was detected with a depth of ∼1.8 ppt. The transit occured ∼12 min late (possibly caused by TTVs, see Section 4.3.3) and the field was cleared of Nearby Eclipsing Binaries in a 5.8 arcsec aperture. An ingress was also observed by the 1.0 m telescope at the Cerro Tololo Inter-American Observatory (CTIO) in Cerro Tololo, Chile (2022 April 01 UT), however, this was not used in subsequent analysis and modelling of the system. TOI-5126 c was also observed with two 1.0 m LCOGT telescopes simultaneously at the Teide Observatory (Teid) in Tenerife, Spain on 2022 April 01 UT. A transit event was detected (∼0.6 ppt) ∼57 min late after double-detrending with a variable aperture of 4.7 and 3.1 arcsec. Two additional full transits of TOI-5126 b were obtained by the 1.0 m telescope at CTIO (2023 February 17 UT & 2023 March 15 UT). Both full coverages resulted in ∼1.2 ppt detections in an uncontaminated 4.7 arcsec aperture. Table 2 provides the details of observation. The phase-folded light curves can be seen in Figure 4.

The images were calibrated by the standard LCOGT BANZAI pipeline (McCully et al. 2018) and differential photometric data

were extracted using AstroImageJ (Collins et al. 2017). We opted to perform our own detrending of all LCOGT light curves simultaneously to the global fit. The trend function for the light curves were represented by a second-order polynomial, with an additional term counting for the full width half-maximum (FWHM) of the PSF. As with the CHEOPS trend model, the coefficients of the detrending vectors were derived from a least squares fit that was performed at each iteration of the global modelling process.

2.2 Reconnaissance spectroscopy

We obtained a series of spectroscopic observations to check for contaminating spectroscopic blend scenarios, and to better constrain the spectroscopic atmospheric parameters of the target star. These reconnaissance spectroscopic observations are detailed in Table 3 and seen in Fig. 5.

We obtained three spectra of TOI-5126 using the Tillinghast Reflector Echelle Spectrograph (TRES; Fűrész, Szentgyorgyi & Meibom 2008) on the 1.5 m telescope at the Fred Lawrence Whipple Observatory (Mt. Hopkins, Arizona). TRES has a resolving power of $R \simeq 44\,000$, with a wavelength coverage of 3850–9096 Å. The observations were obtained with an average exposure SNR
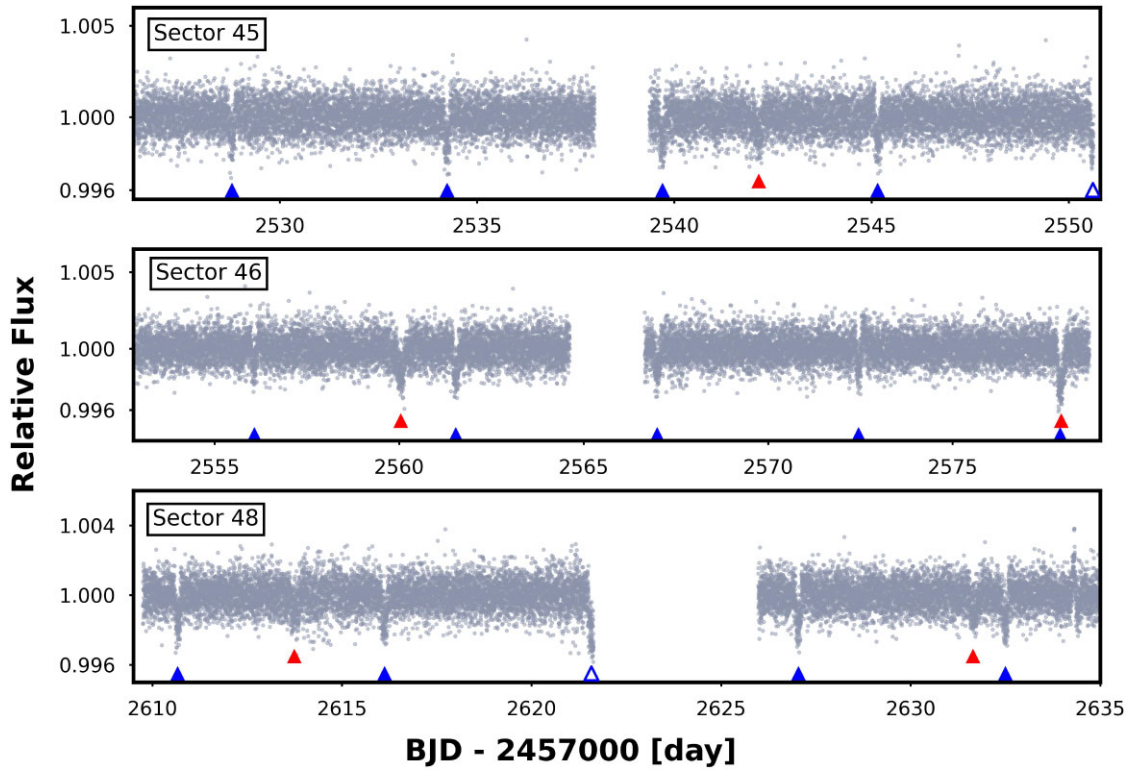
Figure 2. Detrended *TESS* light curve of TOI-5126 from all observed sectors. The light curves are detrended using an iterative B-spline method, and are not used in the global modelilng that lead to the final constraint of the planet parameters. Blue triangles mark each transit of TOI-5126 b, with red arrows for transits of TOI-5126 c. Empty triangles indicate the transits not used in global modelling.
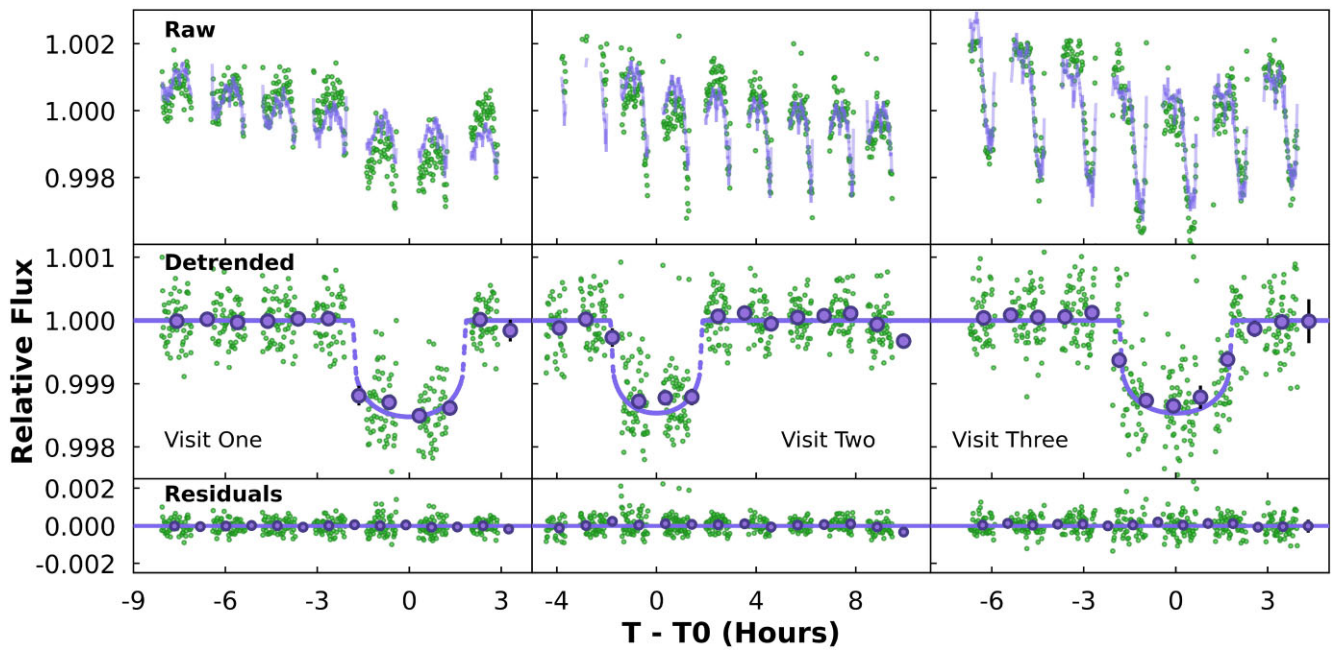

Figure 3. **Upper**: raw normalized *CHEOPS* light curves indicated by green points with the best-fitting trend model plotted in purple. **Middle**: detrended *CHEOPS* light curves shown in green. Binned points are denoted as purple markers and the best-fitting transit model is overplotted as a purple line. **Lower**: residuals of the detrended light curves in green, with binned averaged points shown in purple.

Table 2. SG1 follow-up observations.

Target	Instrument	Date (UT)	Filter	Aperture	Observing notes
TOI-5126 c	LCO-Teid 1.0m	2022-03-10	z_s	5.8 arcsec	Full coverage, simultaneous observation[a]
TOI-5126 c	LCO-Teid 1.0m	2022-03-10	z_s	4.7 arcsec	Full coverage, simultaneous observation[a]
TOI-5126 b	LCO-McD 1.0m	2022-04-01	z_s	5.8 arcsec	Full coverage, simultaneous observation[b]
TOI-5126 b	LCO-McD 1.0m	2022-04-01	z_s	4.7 arcsec	Full coverage, simultaneous observation[b]
TOI-5126 b	LCO-CTIO 1.0m	2022-04-01	z_s	3.9 arcsec	Ingress only, not included in global analysis
TOI-5126 b	LCO-CTIO 1.0m	2023-02-17	z_s	4.7 arcsec	Full coverage
TOI-5126 b	LCO-CTIO 1.0m	2023-03-15	z_s	4.7 arcsec	Full coverage

[a]Transit observed simultaneously by two distinct telescopes at Teid.

[b]Transit observed simultaneously by two distinct telescopes at McD.

Table 3. SG2 reconnaissance spectroscopy.

Telescope	Instrument	Date (UT)	SNR	BJD	RV (km s^{-1})	σ_{RV}
FLWO (1.5 m)	TRES	2022-03-04	40	2459642.86967	0.000[a]	0.063
FLWO (1.5 m)	TRES	2022-03-13	40	2459651.79751	$-$0.071[a]	0.063
FLWO (1.5 m)	TRES	2022-03-24	40	2459662.78279	0.067[a]	0.054
CTIO (1.5 m)	CHIRON	2022-03-02	200	2459640.68363	11.074	0.041
CTIO (1.5 m)	CHIRON	2022-03-20	200	2459658.61297	11.154	0.050
CTIO (1.5 m)	CHIRON	2022-03-22	210	2459660.60426	11.041	0.044
CTIO (1.5 m)	CHIRON	2022-04-15	170	2459684.54751	11.113	0.056
CTIO (1.5 m)	CHIRON	2022-04-16	180	2459685.55202	11.137	0.044

[a]Relative velocities from TRES self-cross correlation analysis.

per resolution element of 38 at 5110 Å. Radial velocities are derived from a multi-order cross correlation analysis as per Quinn et al. (2012), and spectroscopic parameters were derived via the Spectroscopic Parameter Classification tool (Buchhave et al. 2010). Observations yielded stellar parameters for effective temperature ($T_{\mathrm{eff}} = 6217 \pm 50$ K), stellar surface gravity ($\log g = 4.3 \pm 0.1$ cgs), metallicity ([Fe/H] $= 0.17 \pm 0.08$ dex), and projected rotation velocity ($v \sin I_\star = 14.8 \pm 0.5$ km s^{-1}).

In addition, we also obtained five observations of TOI-5126 with the CHIRON high-resolution spectrograph, located on the 1.5 m SMARTS telescope at CTIO, Chile (Tokovinin et al. 2013). Observations were obtained using the fiber fed image slicer, yielding a resolution of $R \sim 80\,000$. The spectra were extracted and reduced via the official CHIRON pipeline (Paredes et al. 2021). Radial velocities were determined from the modelling of their least-squares deconvolution profiles, generated against a non-rotating synthetic template (Zhou et al. 2021). In addition, we also model the rotational broadening of the target as a combination of the rotational, instrument, and macroturbulent broadening kernels. We derive broadening velocities of $v \sin I_\star = 13.2 \pm 0.5$ km s^{-1} and $v_{\mathrm{macro}} = 6.8 \pm 0.5$ km s^{-1} for TOI-5126.

We find no large radial velocity variations at the > 50 m s^{-1} level, or line profile deviations, as is expected for a system of small planets. The results indicate that no obvious spectroscopic blending is present in the system.

2.3 High-resolution imaging

As part of our standard process for validating transiting exoplanets to assess the the possible contamination of bound or unbound companions on the derived planetary radii (Ciardi et al. 2015), we observed TOI-5126 with high-resolution near-infrared adaptive optics (AO) imaging at Palomar Observatory and in the optical with speckle imaging at WIYN and Sternberg Astronomical Institute (SAI). The infrared observations provide the deepest sensitivities to faint companions while the optical speckle observations provide the highest resolution imaging making the two techniques complementary. Combined with *Gaia*, the high-resolution imaging observations find no evidence for additional stellar companions within the system.

2.3.1 Palomar 5m/PHARO

The Palomar Observatory observations were made with the PHARO instrument (Hayward et al. 2001) behind the natural guide star AO system P3K (Dekany et al. 2013) on 2022 February 13 UT in a standard 5-point quincunx dither pattern with steps of 5 arcsec in the narrow-band $B r - \gamma$ filter ($\lambda_o = 2.1686$; $\Delta\lambda = 0.0326$ μm). Each dither position was observed three times, offset in position from each other by 0.5 arcsec for a total of 15 frames; with an integration time of 5.7 s per frame, the total on-source time was 85.5 s. PHARO has a pixel scale of 0.025 arcsec pixel^{-1} for a total field of view of $\sim$25 arcsec. The science frames were flat-fielded and sky-subtracted. The reduced science frames were combined into a single combined image with a final resolution of 0.97 arcsec FWHM.

To within the limits of the AO observations, no stellar companions were detected. The sensitivities of the final combined AO image were determined by injecting simulated sources azimuthally around the primary target every 20° at separations of integer multiples of the central source's FWHM (Furlan et al. 2017; Lund & Ciardi 2020). The brightness of each injected source was scaled until standard aperture photometry detected it with $5 - \sigma$ significance. The resulting brightness of the injected sources relative to TOI 5126 set the contrast limits at that injection location. The final $5 - \sigma$ limit at each separation was determined from the average of all of the determined limits at that separation and the uncertainty on the limit was set by the rms dispersion of the azimuthal slices at a given radial distance. Fig. 6 shows no stellar companion with a difference in magnitude (Δmag) of 5.4 at a separation $\sim$0.3 arcsec, and all companions ruled out in a contrast of Δmag of 9 from $\sim$2 arcsec
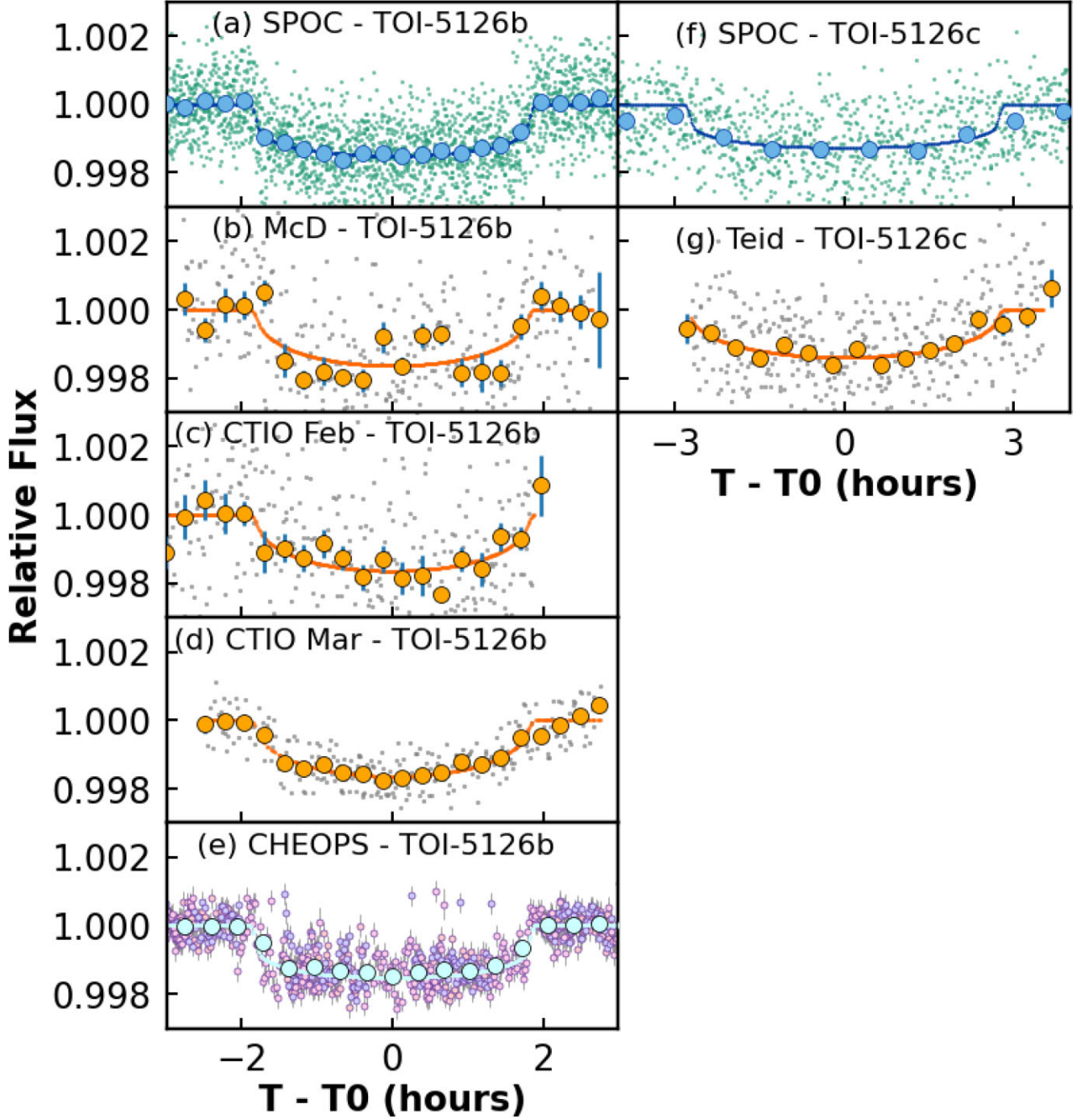
Figure 4. Phase-folded light curves of TOI-5126 b and TOI-5126 c. *TESS* SPOC light curves are noted by green points, with binned data in blue and the best-fitting transit model line in blue. LCOGT data is represented by grey points with orange binned points and errorsbars in blue. The transit model is also denoted as an orange line. The *CHEOPS* phase-folded light curve is combined with all three visits TOI-5126 b, where the purple, pink, and blue points represent each visit, respectively. The binned data is in cyan, with the transit model also a cyan line. (a)*TESS* SPOC TOI-5126 b. (b) McD TOI-5126 b. (c) CTIO 2022 TOI-5126 b. (d) CTIO 2023 TOI-5126 b. (e) CHEOPS combined visits of TOI-5126 b. (f)*TESS* SPOC TOI-5126 c. (g) Teid TOI-5126 c.

onwards. No sources are present in the field of view with an upper limit on the angular separation of 4 arcsec.

2.3.2 WIYN 3.5m/NESSI

Further imaging observations were made using the NN-Explore Exoplanet Stellar Speckle Imager (NESSI; Scott et al. 2018) on the WIYN 3.5 m telescope at the Kitt Peak National Observatory in Arizona. The observation and data reduction of NESSI can be found in Howell et al. (2011). Images were taken at 832 nm on UT 2022 April 18. The 5-σ sensitivity curve, imaged in Fig. 6, outline a Δm of 6 from 0.96 arcsec onwards. The inset image (1.2 arcsec angular separation) also shows no stellar neighbours within the Δm of 6.
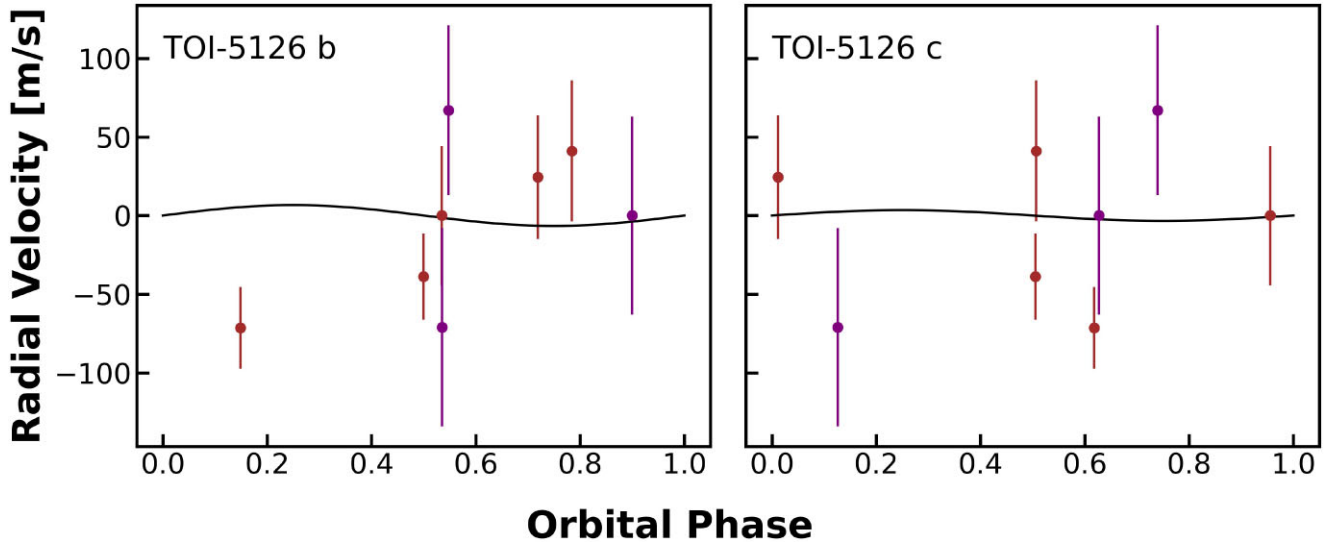
Figure 5. *Left*: radial velocities against the orbital phase of TOI-5126 b with the notional K semi-amplitude curve based off of predicted mass in Section 4.5. TRES points are represented by purple points, while CHIRON data is in brown. **Right**: radial velocities versus orbital phase for TOI-5126 c. with notional K semi-amplitude curve drawn from predicted mass.
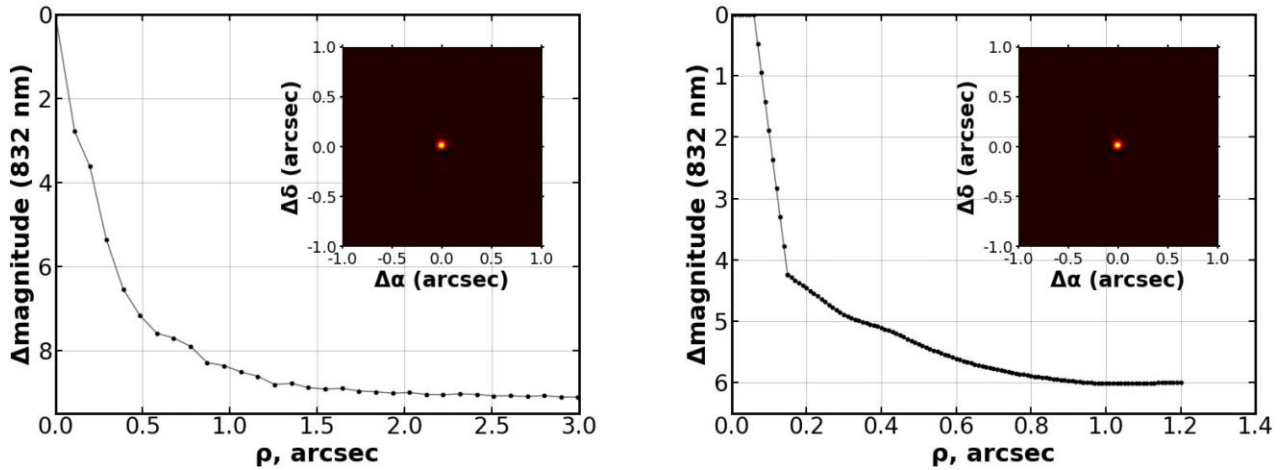

Figure 6. *Left*: Palomar 5.0 m companion sensitivity curve. The black points represent the 5-σ limits. The inset image is of the primary target showing no additional close-in companions. *Right*: contrast curve of TOI-5126 with the NESSI instrument on the WIYN 3.5 m telescope, reaching a constrast of Δ 6 mag from 0.96 arcsec.

2.3.3 SAI 2.5m/Speckle Polarimeter

A third direct image of TOI-5126 was taken using the Speckle Polarimeter on the 2.5 m SAI (Safonov, Lysenko & Dodin 2017). Observations were made in the I_c filter ($\approx$660–825 nm). Observations were in agreement with the prior direct imaging observations, reaching a contrast of Δm of 7 from 1 arcsec.

2.3.4 Gaia Assessment

In addition to the high-resolution imaging, we have utlized *Gaia* to identify any wide stellar companions that may be bound members of the system. Typically, these stars are already in the TESS Input Catalog and their flux dilution to the transit has already been accounted for in the transit fits and associated derived parameters. Based upon similar parallaxes and proper motions (e.g.

Mugrauer & Michel 2020, 2021; Mugrauer, Zander & Michel 2022), there are no additional widely separated companions identified by *Gaia*.

Additionally, the *Gaia* DR3 astrometry provides additional information on the possibility of inner companions that may have gone undetected by either *Gaia* or the high-resolution imaging. The Gaia Renormalised Unit Weight Error (RUWE) is a metric, similar to a reduced χ^2, where values that are $\lesssim 1.4$ indicate that the *Gaia* astrometric solution is consistent with the star being single whereas RUWE values $\gtrsim 1.4$ may indicate an astrometric excess noise, possibly caused the presence of an unseen companion (e.g. Ziegler et al. 2020). TOI-5126 has a *Gaia* DR3 RUWE value of 1.16 indicating that the astrometric fits are consistent with the single star model. In addition the *GAIA* DR3 non-single-star flag is no present for the system, implying further that this is a single star system.
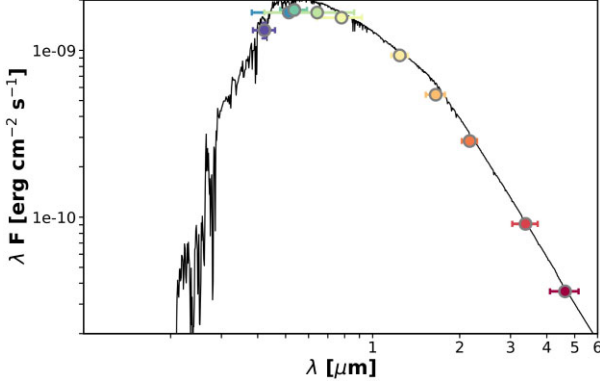
Figure 7. Spectral energy distribution (SED) of TOI-5126. Circles indicate the photometric bands with horizontal bars reflecting the passband width.

3 ANALYSIS

3.1 Stellar parameters

Stellar parameters for TOI-5126 were obtained by fitting the star's broad-band spectral energy distribution (SED) to stellar atmosphere models using the Python package ASTROARIADNE (Vines & Jenkins 2022). We used TRES spectroscopic data to define priors on the stellar effective temperature (T_{eff}) (with its uncertainty inflated to 150 K) and metallicity (Fe/H), while distance constraints were derived from *Gaia* DR3 parallax (Gaia Collaboration 2022). We used the default prior for Extinction (A_v) which constrains an upper limit using the SFD galactic dust maps from Schlegel, Finkbeiner & Davis (1998).

ASTROARIADNE uses a Bayesian Model Averaging approach, fitting multiple models[3] accounts for model-specific systematic biases. Each model is weighed individually for a combined weighted and averaged posterior probability. This is then fed into the isochrone fitting package. In SED fitting (see Figure 7), we used Tycho-2 (Høg et al. 2000) *B* and *V*, Gaia DR3 (Fabricius et al. 2021) *G*, B_p and R_p, Two-Micron All-Sky Survey (2MASS) (Skrutskie et al. 2006) *J*, *H*, *K*, and Wide-field Infrared Survey Explorer (WISE) (Wright et al. 2010) W_1 and W_2 bands, with an uncertainties floor applied to all bands based on Eastman et al. (2019). The weighted average results obtained are $T_{eff} = 6150^{+130}_{-100}$ K, $\log g = 4.31^{+0.24}_{-0.23}$ cgs, $R_\star = 1.249^{+0.040}_{-0.038}$ R$_\odot$, and [Fe/H] $= 0.18^{+0.13}_{-0.13}$ dex. The full stellar parameters can be seen in Table 4.

To identify the rotation period of TOI-5126, we passed the raw deblended SPOC light curve through a Lomb–Scargle periodogram. The highest power of the entire *TESS* set of observations was constrained to be $4.602^{+0.071}_{-0.067}$ d. We used the FWHM of the highest power to derive our uncertainties. We also measured the Lomb–Scargle peaks of each sector separately, finding a scatter in the derived rotation period of $\sigma = 0.066$ d, consistent with the uncertainty estimated from the peak FWHM. However, the actual uncertainty of the rotation period may be much larger and is difficult to quantify with the short observational baseline available. The periodogram can be seen in Fig. 8. Given the system has a measured $v \sin I_\star$ of ~ 14 km s^{-1}, the inclination of the star is consistent with 90 degrees.

---

[3]The models used for this specific fit are: Phoenixv2 (Husser et al. 2013), BT-Settl (Allard, Homeier & Freytag 2012), BT-NextGen (Allard et al. 2012), BT-Cond (Hauschildt et al. 1999; Allard et al. 2012), and Kurucz93 (Kurucz 1993)
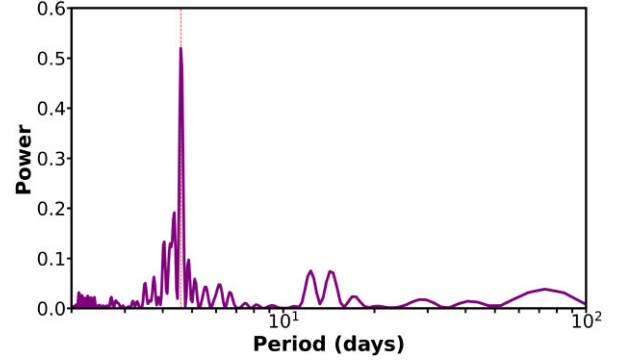

Figure 8. Lomb–Scargle periodogram of the raw SPOC TOI-5126 light curve. The highest-power period is denoted by a dashed line. Uncertainties are derived from FWHM of the highest-power resulting in a period of $4.602^{+0.071}_{-0.067}$ d.

3.2 Global modelling

To characterize the physical parameters of the TOI-5126 system, along with their associated uncertainties, we performed a Markov Chain Monte Carlo fit using the publicly available software package EMCEE (Foreman-Mackey et al. 2013). We opted to not include the 2022 April 01 CTIO observation of TOI-5126 b in our fit because it only captured an ingress. Detrending was performed simultaneously to the transit fits for each photometric observation. During each iteration, we subtracted a transit model created from the BATMAN package (Kreidberg 2015) from the observed data. Next, we fit a trend model to the residuals using least-squares optimization, and compared the best trend model and the residuals to determine the log likelihood for the sampler. Section 2 contains further information on the individual trend models.

The global modelling process involved fitting for the two planets simultaneously. Our fit included the period, epoch, the planet-to-star radius ratio, $R_p/R_\star$ and impact parameter, b of both planets. Eccentricities were initially fixed at 0 as we assumed a circular solution. The limb darkening coefficients for each unique photometric filter, denoted as $q_{1,i}$ and $q_{2,i}$, were included in the global fit. These coefficients were parameterized as per Kipping (2013). Additionally, we included a scaling factor for each observation as a free parameter in the fit, c_i. This accounts for differing levels of background contamination due to the varying apertures of the individual instruments. This parameter is neccessary as the large PSFs of both *TESS* and *CHEOPS* allow background stars to contribute to the measured flux, resulting in differing total fluxes to that of the LCOGT light curves. We also opted to fit for $M_\star$ and $R_\star$ to simultaneously constrain them with the planet parameters.

To constrain the period and transit times of both planets, we imposed uniform priors with boundaries at the 5-σ upper and lower uncertainty provided by the SPOC detection pipeline. For *TESS* and *CHEOPS*, we allow the c values to uniformly explore between boundaries of 0.9–1.1, this is due to the brightest contaminating star in TESS/CHEOPS aperture account for roughly 5 per cent of the light of the target star. Since the LCOGT aperture excluded all neighbouring stars resolved by the *Gaia* catalogue, we tightly constrain c_{lco} to only uniformly vary between 0.99 and 1.01. For $M_\star$ and $R_\star$, we imposed a Gaussian prior derived from the results of the SED fitting obtained in Section 3.1.

We first assumed the orbits of the two planets to be circular. We also ran a set of global modelling allowing non-zero eccentricities for both planets. Our eccentric fit consisted of all previously mentioned

Table 4. Stellar parameters for TOI-5126.

Parameter	Value	Source
Catalogue information		
RA (h:m:s)	10:06:38.34	Gaia DR3
Dec. (d:m:s)	+18:38:02.62	Gaia DR3
Epoch	2016.0	Gaia DR3
Parallax (mas)	6.224 ± 0.022	Gaia DR3
μ_{ra} (mas yr^{-1})	-54.700 ± 0.022	Gaia DR3
μ_{dec} (mas yr^{-1})	-10.4043 ± 0.016	Gaia DR3
Gaia DR3 ID	623633615066248576	
TIC ID	27064468	
TOI ID	5126	
Photometric properties		
TESS (mag)	9.5622 ± 0.0064	TIC v8.2
Gaia (mag)	9.946 ± 0.006	Gaia DR3
Gaia RP (mag)	9.519 ± 0.012	Gaia DR3
Gaia BP (mag)	10.222 ± 0.013	Gaia DR3
V_J (mag)	10.141 ± 0.006	APASS DR10
B_J (mag)	10.573 ± 0.108	APASS DR10
J (mag)	9.043 ± 0.018	2MASS
H (mag)	8.845 ± 0.015	2MASS
K_s (mag)	8.777 ± 0.018	2MASS
W_1 (mag)	8.712 ± 0.03	WISE
W_2 (mag)	8.743 ± 0.03	WISE
Derived properties		
$M_\star$ (M$_\odot$)	$1.240^{+0.050}_{-0.046}$	Constant period circular fit
$R_\star$ (R$_\odot$)	$1.241^{+0.032}_{-0.027}$	Constant period circular fit
$\log g_\star$ (cgs)	$4.224^{+0.051}_{-0.062}$	Constant period circular fit
$L_\star$ (L$_\odot$)	$1.99^{+0.18}_{-0.17}$	Constant period circular fit
$T_{eff\star}$ (K)	6150^{+110}_{-130}	SED
[*Fe/H*] (dex)	$0.18^{+0.13}_{-0.13}$	SED
Distance (pc)	161.1 ± 1.2	SED
$\rho_\star$ (g cm^{-3})	$0.922^{+0.065}_{-0.079}$	Constant period circular fit
Age (Gyr)	$0.8^{+2.8}_{-0.7}$	SED
Limb-darkening coefficients		
$u_{1,TESS}$	$0.25^{+0.17}_{-0.17}$	
$u_{2,TESS}$	$0.34^{+0.25}_{-0.19}$	
u_{1,z_s}	$0.56^{+0.33}_{-0.39}$	
u_{2,z_s}	$0.26^{+0.33}_{-0.39}$	
$u_{2,CHEOPS}$	$0.09^{+0.29}_{-0.21}$	
$u_{2,CHEOPS}$	$0.09^{+0.29}_{-0.21}$	
Scaling coefficients		
c_{TESS}	$1.056^{+0.023}_{-0.045}$	
c_{McD}	$1.0001^{+0.0070}_{-0.0063}$	
c_{Teid}	$0.9986^{+0.0075}_{-0.0060}$	
$c_{CTIO,1}$	$0.998^{+0.010}_{-0.005}$	
$c_{CTIO,2}$	$0.9963^{+0.0084}_{-0.0044}$	
$c_{CHEOPS,1}$	$1.075^{+0.017}_{-0.040}$	
$c_{CHEOPS,2}$	$1.011^{+0.052}_{-0.035}$	
$c_{CHEOPS,3}$	$1.064^{+0.025}_{-0.036}$	

free parameters, as well as the addition of $\sqrt{e}\cos\omega$ and $\sqrt{e}\sin\omega$ as free parameters, where e is the eccentricity and ω is the longitude of periastron. These parameters could be derived to find the eccentricity and longitude of periastron of both planets. The results of both fits can be seen in Table 5.

Through visual examination of the detrended light curves against the models, assuming a constant period, we noticed that both planets deviated slightly from their predicted transit timing assuming they are both on circular orbits. We followed the algorithm outlined in Nabbie et al. (in preparation) to search for potential TTVs. The 2022 April 01 CTIO observation of TOI-5126 b and Teid observation of TOI-5126 c were excluded due to their insufficient out-of-transit

baselines. For the rest of the transits, we fit for their individual transit centres independently while allowing for the trend parameters to vary similarly to the previous model. Instead of using Gaussian priors on the stellar parameters, we added the likelihood term from the SED in our model instead so that all the stellar parameters can be constrained at the same time as the transit parameters.

For the SED likelihood, we make use of the isochrone package (Morton 2015) and the MIST tracks. We fixed stellar parallax, distance, and reddening to the best-fitting values from 3.1. We added T_{eff}, [Fe/H] and age as our free parameters, and an error scale parameter following Eastman et al. (2019). The priors of T_{eff} and [Fe/H] are constrained by Gaussian priors with uncertainties

Table 5. Planet parameters for TOI-5126.

Parameter	Constant period			
	Circular		Eccentric	
	TOI-5126 b	TOI-5126 c	TOI-5126 b	TOI-5126 c
Light-curve parameters				
P (d)	$5.4588385^{+0.0000070}_{-0.0000072}$	$17.8999^{+0.0018}_{-0.0013}$	$5.4588382^{+0.0000070}_{-0.0000070}$	$17.8999^{+0.0020}_{-0.0012}$
$T_{\rm c}$ (BJD − 2457000) .	$2627.03862^{+0.00043}_{-0.00039}$	$2613.7443^{+0.0049}_{-0.0029}$	$2627.03862^{+0.00049}_{-0.00045}$	$2613.7440^{+0.0051}_{-0.0023}$
T_{14} (h)	$3.726^{+0.017}_{-0.016}$	$5.34^{+0.14}_{-0.17}$	$3.72^{+0.14}_{-0.17}$	$5.25^{+0.34}_{-0.57}$
$T_{12} = T_{34}$ (min)	$8.00^{+0.54}_{-0.44}$	$9.97^{+0.85}_{-0.71}$	$8.08^{+0.62}_{-0.40}$	$10.3^{+2.5}_{-1.0}$
$a/R_\star$	$11.32^{+0.26}_{-0.33}$	$24.99^{+0.57}_{-0.74}$	$11.26^{+0.33}_{-0.36}$	$24.85^{+0.73}_{-0.79}$
$R_{\rm p}/R_\star$	$0.03498^{+0.00065}_{-0.00060}$	$0.02854^{+0.00080}_{-0.00090}$	$0.03511^{+0.00063}_{-0.00058}$	$0.0287^{+0.0016}_{-0.0010}$
$b \equiv a\cos i/R_\star$	$0.24^{+0.10}_{-0.14}$	$0.34^{+0.10}_{-0.14}$	$0.24^{+0.15}_{-0.14}$	$0.38^{+0.20}_{-0.23}$
i (deg)	$88.79^{+0.72}_{-0.53}$	$89.23^{+0.32}_{-0.25}$	$88.82^{+0.69}_{-0.82}$	$89.13^{+0.53}_{-0.49}$
e	0 (Fixed)	0 (Fixed)	$0.09^{+0.21}_{-0.07}$	$0.21^{+0.40}_{-0.16}$
ω (deg)	0 (Fixed)	0 (Fixed)	-10^{+110}_{-130}	-20^{+130}_{-120}
Planetary parameters				
$R_{\rm p}$ ($R_\oplus$)	$4.74^{+0.16}_{-0.14}$	$3.86^{+0.17}_{-0.16}$	$4.76^{+0.17}_{-0.15}$	$3.90^{+0.26}_{-0.18}$
a (AU)	$0.06519^{+0.00087}_{-0.00082}$	$0.1439^{+0.0019}_{-0.0018}$	$0.0650^{+0.0011}_{-0.0009}$	$0.1435^{+0.0025}_{-0.0020}$
$T_{\rm eq}$ (K)	1442^{+46}_{-40}	971^{+31}_{-27}	1445^{+52}_{-46}	972^{+35}_{-31}
$\langle F \rangle$ ($S_\oplus$)	467^{+44}_{-39}	96^{+9}_{-8}	471^{+48}_{-44}	97^{+10}_{-9}

provided by Section 3.1. We adopt uniform priors for $M_\star$ and $R_\star$ with bounds between 1 and 1.4. The error scale was bounded between 0.01 and 100, and stellar age between 0.5 and 10 Gyr.

4 RESULTS AND DISCUSSION

4.1 Global modelling results

Through the results of our analysis conducted in Section 3.2, we report the discovery and validation of two planets around the bright F star TOI-5126. We have determined TOI-5126 b to be a hot super-Neptune, with a radius of $4.74^{+0.16}_{-0.14}$ $R_\oplus$ in a $5.4588385^{+0.0000070}_{-0.0000072}$ day orbit. Further, we have discovered and validated TOI-5126 c as a warm Neptune at $3.86^{+0.17}_{-0.16}$ $R_\oplus$. TOI-5126 c orbits its host star every $17.8999^{+0.0018}_{-0.0013}$ d. Comparison with the current exoplanet demographic is found in Fig. 11. The full parameter results are presented in Table 5. The eccentric fit and the circular fit have predominantly overlapped posterior space. We have also detected a tentative TTV signal which will be discussed in Section 4.3.3. As expected, the best-fitting parameters retrieved when allowing the transit times to vary in the global model, produced slightly larger transit depths and shorter transit durations for both planets. However, the joint modelling with the SED lead to a slightly smaller stellar radius. The posterior of the final planet parameters largely overlap, with the TTV fit reports TOI-5126 b having a radius of $4.67^{+0.14}_{-0.13}$ $R_\oplus$ and a transit duration of $3.686^{+0.032}_{-0.026}$ h. For TOI-5126 c, the TTV fit reports a radius of $3.76^{+0.14}_{-0.13}$ $R_\oplus$ and a transit duration of $5.46^{+0.10}_{-0.16}$ h.

4.2 Validation of the TOI-5126 system

Both astrophysical phenomena and instrumental artifacts can replicate the signal of a planetary transit. Without careful consideration of false positive scenarios, the legitimacy of the planet can be compromised. In this section, we validate the TOI-5126 system by ruling out false positive scenarios which could have created the observed transit signals. We consider the following scenarios:

(i) **Either of the transit signals are a reflection of instrumental artifact:** Both transit signals were detected with high significance in the *TESS* data, *CHEOPS* and ground-based telescopes as mentioned in Section 2.1.3, therefore this possibility is ruled out.

(ii) **TOI-5126 is an eclipsing binary**: This scenario is ruled out by our radial velocity observations from TRES and CHIRON (section §2.2). An analysis on the system shows that a brown dwarf companion ($M_{\rm p} \approx 13 M_{\rm Jup}$) orbiting around TOI-5126 would produce RV semi-amplitudes of $K_{\rm b} = 1326$ m s^{-1} and $K_{\rm c} = 892$ m s^{-1}. Neither sets of the radial velocity observations show such deviations.

(iii) **Light from a distant eclipsing binary or transiting planet system is blended with TOI-5126**: The magnitude difference between TOI-5126 and the faintest companion which could replicate the signals observed follow as: $\Delta m \lesssim 2.5 \log 10 \left(\frac{t_{12}^2}{t_{13}^2 \delta_{\rm obs}} \right)$. The faintest star which could replicate the transit signals for TOI-5126 b is $\Delta m = 7$, and TOI-5126 c is $\Delta m = 6$. Direct imaging observations rule out stars with a Δm of 7 from 0.5 arcsec onwards, and ground-based photometric observations detected the transit events within a 4.7 arcsec aperture. To statistically rule out stars within 0.5 arcsec of TOI-5126, we determined the average stellar density in the nearby field from *Gaia* data. For stars within a magnitude range of seven magnitudes, the average stellar density is calculated to be 2.4×10^{-5} arcsec^{-2}. Narrowing this caclulation to stars six magnitudes fainter than TOI-5126, the average stellar density is 4.0×10^{-5} arcsec^{-2}.

An additional investigation into the probability of remaining false positive scenarios was performed using TRICERATOPS (Giacalone & Dressing 2020). We used the detrended *TESS* light curves of TOI-5126 b and TOI-5126 c, as well as constraints provided by Palomar imaging (see Section 2.3) in our analysis. A false-positive probability (FPP) of 0.77 per cent and a nearby false-positive probability (NFPP) of 0 per cent offer statistical validation for TOI-5126 b. Analysis of the *TESS* light curve for planet c reveals a FPP and NFPP of 5.33 per cent and 4.98 per cent, respectively. This is invoked by a Nearby Eclipsing Binary scenario on 9.53 arcsec away neighbour
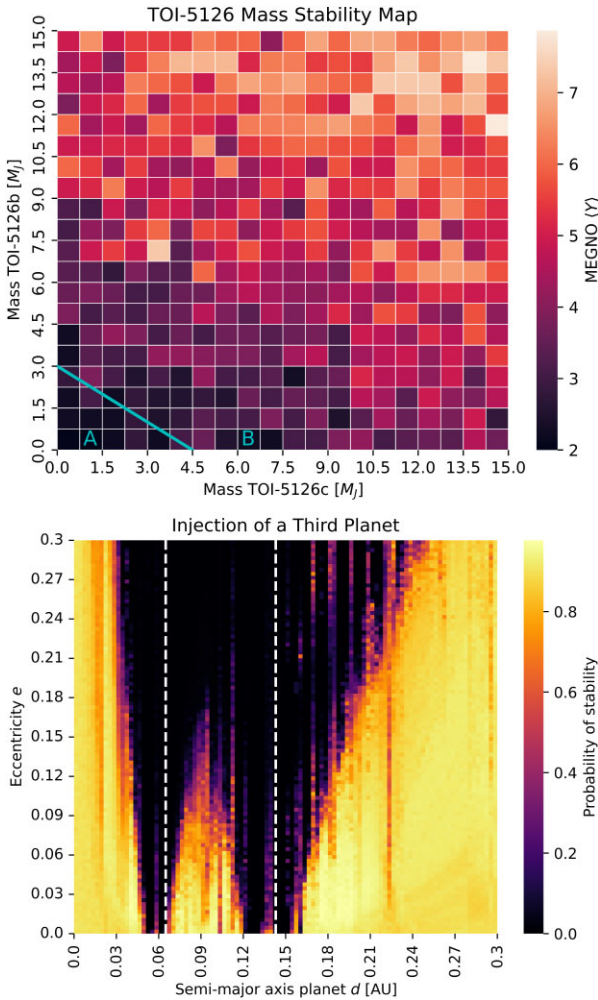
Figure 9. *Top*: MEGNO stability map in the M_b–M_c parameter space. Two distinct regions of stability are divided by the solid cyan line, with the region A below the line indicate stable configurations. Each pixel in the 20×20 map holds the average of 30 realizations of randomized initial conditions. *Bottom*: stability map generated using SPOCK for a hypothetical third planet within the TOI-5126 system. The vertical white dashed lines denote the locations of TOI-5126 b and TOI-5126 c. Each cell in the map represents the average of 10 realizations with randomized initial conditions. There is a small stable region present between the two planets in which a hypothetical third planet could reside.

TIC27064467. This scenario, however, has been ruled out by the on-target event detected by ground-based photometry. As a result, the FPP with this scenario eliminated is 0.35 per cent.

4.3 Dynamical constraints on the system

4.3.1 Long-term stability

The masses and eccentricities of the planets are currently not well-constrained. In this section, we explore the possibility of placing additional constraints on the system through considerations of long-term dynamical stability. We first assess the stability of the observed system using calculations of the Mean Exponential Growth factor of Nearby Orbits (MEGNO; Cincotta & Simó 2000; Cincotta, Giordano & Simó 2003) indicator within the REBOUND gravitational dynamics software package (Rein & Liu 2012a). For a given set of

initial conditions, we quantify the stability of the system using the time-averaged MEGNO chaos indicator value, $\langle Y(t) \rangle$, which reflects the degree of divergence of initially closely separated trajectories in phase space. Stable system configurations will have MEGNO values $\lesssim 2$.

The MEGNO value across a grid of different masses for both planets is displayed in the top panel of Fig. 8. We are able to obtain a relatively loose constraint on the planet masses: approximately, if $M_b + \frac{2}{3} M_c < 3M_J$, the system will be stable. To estimate the average MEGNO value in each cell, we randomly sample the initial condition 30 times. We assume eccentricities of both planets were randomly drawn from a Rayleigh distribution with scale parameter 0.1. The mean anomaly and argument of periapse angles are sampled uniformly between 0 and 2π. The integration time for each realization was set to 10^6 orbits of the outermost planet with a time-step of 1/20th of the innermost planet's period.

We also found the system will be stable across a wide range of eccentricities for both planets if their masses approximated by the mass–radius relationship following Otegi, Bouchy & Helled (2020). Therefore, the stability criterion alone cannot provide additional constraint on the system eccentricity.

4.3.2 Stability of a hypothetical third planet

The two detected planets in the TOI-5126 system are fairly widely spaced ($P_c/P_b \sim 3.3$). It is possible that there is a third planet residing between the orbits of the two planets or somewhere else in the system. To explore this possibility, we use the Stability of Planetary Orbital Configurations Klassifier (SPOCK; Tamayo et al. 2020) to compute the probability of stability of a given set of parameters. SPOCK is a machine learning model trained on $\sim 100\,000$ orbital configurations of three-planet systems. It can estimate the probability of long-term stability of planetary systems with three or more planets.

In particular, we explored the $a_d - e_d$ space of the additional planet, whose mass we set to the average of the nominal masses of planets b and c based on the mass–radius relationship discussed in Section 4.3.1. We assumed circular orbits for planets b and c while varying the eccentricity of planet d from 0 to 0.3 and semi-major axis from 0 to 0.3 AU. Setting the orbits of the known planets to circular provides us with the maximum possible stable region for the hypothetical third planet. Each grid cell in the a_d–e_d map represents the average of 10 realizations of the system with randomized initial conditions. Specifically, the mean anomalies, longitudes of ascending nodes, and inclinations were randomly drawn according to M, $\omega \sim$ Unif$[0, 2\pi]$, $i \sim$ Rayleigh($1°$).

The bottom panel of Fig. 9 shows the results of the SPOCK stability map for a hypothetical third planet. In addition to stable regions interior to TOI-5126 b and exterior to TOI-5126 c, there is also a stable region between the two planets. It is possible that a planet may be transiting but remain undetected due to its small radius. Alternatively, the planet could also be either non-transiting or in the trivial case not exist at all. Nevertheless, Fig. 9 indicates the ideal orbital proximity in which to search for additional planets in the system.

4.3.3 Transit timing variations signal in the light curves

From our analysis of the *TESS* light curves, we find that both planets exhibit tentative TTVs, seen in Fig. 10. Such signals can potentially arise due to the gravitational perturbations that the planets impart on
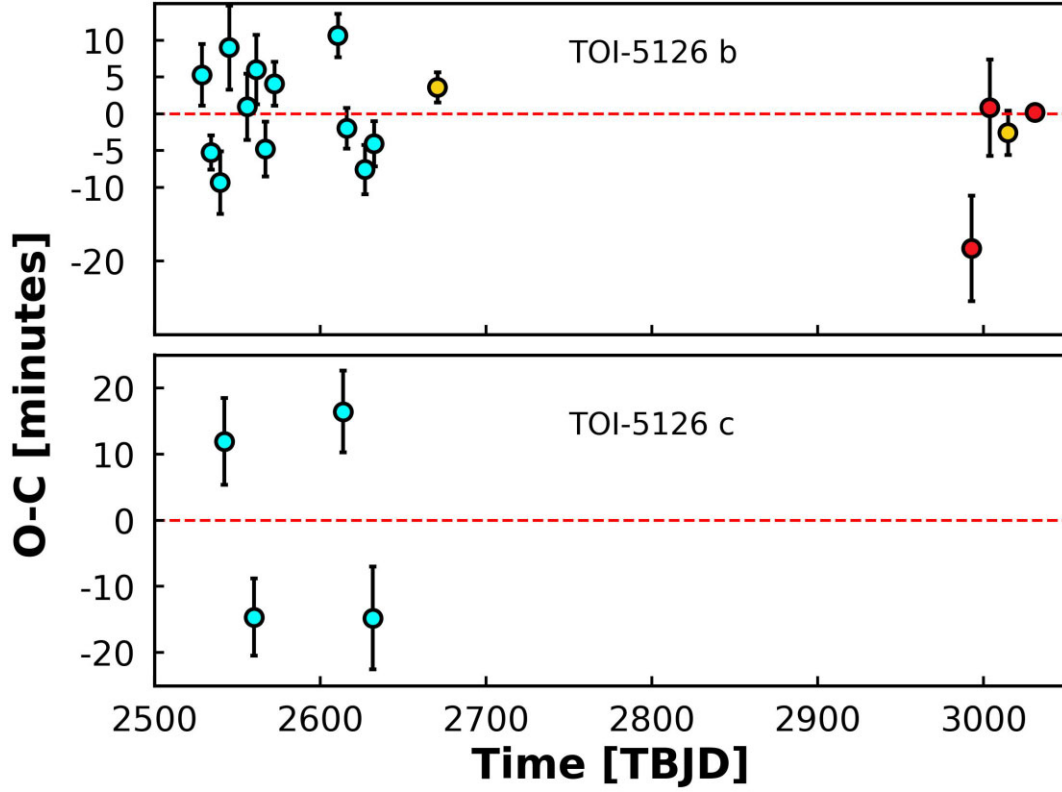
Figure 10. Transit times subtracted from a linear ephemeris for TOI-5126 b and TOI-5126 c. Cyan indicates *TESS* transits, yellow indicates LCOGT transits, and red indicates *CHEOPS* transits. The red dashed line shows the expected transit time assuming a constant period.
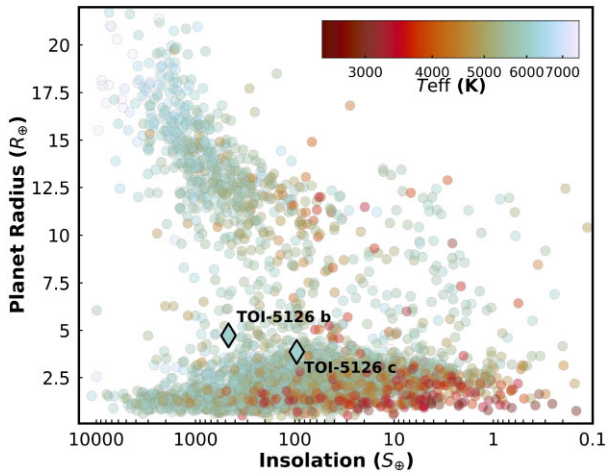

Figure 11. Radius relative to insolation flux for the population of confirmed planets. Colours represent the host star effective temperature. Plots were made with data downloaded from NASA exoplanet archive on 2023 February 07 UT.Radius relative to insolation flux for the population of confirmed planets. Colours represent the host star effective temperature. Plots were made with data downloaded from NASA exoplanet archive on 2023 February 07 UT..

Figure 12. Radius ratios of all known inner/outer planet pairs as a function of their insolation ratios. The colours represent the inner planets' insolation flux in Earth units. The horizontal dashed line at one represents a same sized planet pair, with the arrow outlining the decrease in radius ratio expected by photoevaporation of the inner hotter planet. This plot makes use of data from the NASA exoplanet archive (Akeson et al. 2013) downloaded on 2023 February 07 UT. The data extracted only planets with measured periods, radii and host star masses, radii and effective temperatures known.

one another as they reach conjunction, creating non-periodic transit times. Notably, TOI-5126 b and TOI-5126 c are not near a first-order mean-motion resonance, which would produce the largest TTV amplitudes (Agol et al. 2005).

We utilized REBOUND (Rein & Liu 2012a) to estimate expected TTV signals based on TOI-5126 b and TOI-5126 c alone. We sample

the initial orbital elements of both planets (a, e, w, i) from the posterior distribution results from our global models (including the TTV fit) in Section 3. The other orbit angles are sampled uniformly

between 0 and 2π. The systems are integrated for more than 500 d and transit times corresponding to the observed transits from *TESS*, LCO, and *CHEOPS* are recorded. The expected TTV scatter is then computed by calculating the standard deviation of the transit times after subtracting the best-fitting linear ephemeris. We simulated the system for 10 000 realizations and found that TOI-5126 b produced 2-σ upper limit variations of 0.27 min, with TOI-5126 c exhibiting 0.19 min 2-σ upper limit TTVs. The current system is therefore unable to explain the observed TTVs and we consider alternate scenarios.

One possible interpretation is that these signals imply the existence of a third, non-transiting planet in between TOI-5126 b and TOI-5126 c (as discussed in the previous section), so that one of the neighbouring planet pairs have a period ratio just wide of a 3:2 resonance and the other just wide of a 2:1 resonance, both of these period ratios being commonly found in multi-planet systems (Fabrycky et al. 2014).

However, we caution that it has been shown in previous studies that spot crossing events can mimic TTV signals rather than gravitational interactions due to planets (Sanchis-Ojeda et al. 2011; Fabrycky et al. 2012; Mazeh et al. 2013; Szabó et al. 2013), especially when the individual transit has relatively low signal-to-noise. Ioannidis, Huber & Schmitt (2016) demonstrated that an SNR larger than 15 is required to statistically minimize the probability that a spot crossing event being the cause of the deviations. The SNR of planet b in *TESS* data is 13, with planet c having an SNR of 11. Given two out of three of our CHEOPS observations does not cover either ingress or egress of the transits, further high signal-to-noise photometry follow-up is needed to unlock the full system architecture of TOI-5126.

4.4 TOI-5126 b in context with the super-Neptune population

TOI-5126 b is the newest addition to the super-Neptune population, the class of planets with radii between 4 and 8 $R_\oplus$, and diverse compositions (with mass ranging between 6 and 135 $M_\oplus$; Akeson et al. 2013). TOI-5126 b's planetary parameters ($R_b \approx 4.7$ $R_\oplus$, $P_b \approx 5.46$ d) place it in the sparsely populated $\lesssim 10$ d, 4–8 $R_\oplus$ region of the period–radius plane, known as the 'hot Neptune desert' (Mazeh et al. 2016) (see Fig. 11).

The unusually large radius of TOI-5126 b implies that long-term mass-loss processes are likely still ongoing and may be readily observable. Of all super-Neptunes in the desert, TOI-5126 b is on an exclusive list of three (WASP-166 b, Hellier et al. 2019; LTT 9779 b, Jenkins et al. 2020b) with visual magnitudes $\lesssim 10$ and predicted equilibrium temperatures above the cloud-free threshold ($\gtrsim 1200$ K). This makes it one of the most readily characterizable highly irradiated super-Neptune's for transmission spectroscopic observations, where mass-loss mechanisms can be directly probed. Questions surrounding mass-loss are particularly unique for TOI-5126 as planet b is larger than planet c, despite receiving more stellar irradiation. This is in contrast to the expected outcome of photoevaporation, which implies that the inner companion would be smaller if the insolation ratio is larger. An example of the radius and insolation ratio relation, as well as the expected outcome of photoevaporation, can be seen in Fig. 12.

4.5 Other future follow-up opportunities

We compute predicted masses for TOI-5126 b and c based on the mass–radius relationship from Otegi et al. (2020). These predicted
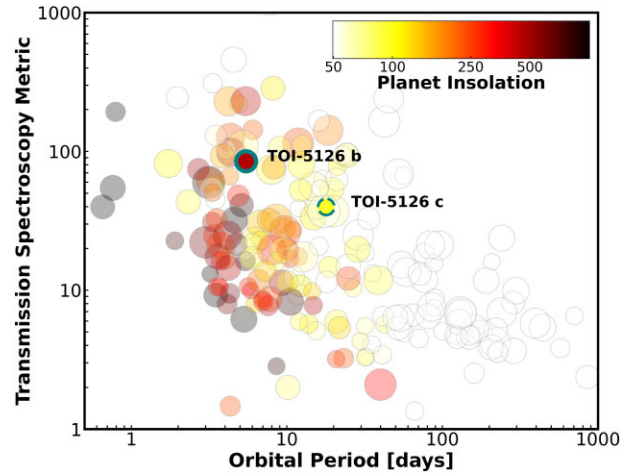

Figure 13. TOI-5126 planets among all super-Neptunes in terms of orbital period and TSM. TOI-5126 c is notably not a super-Neptune and is outlined for comparative purposes as a dashed line. The colour of each point describes the planets' insolation flux, with point size representing their scaled radius. This plot makes use of data from the NASA exoplanet archive downloaded on 2023 February 07 UT.

masses are adopted for the discussions below. The predicted masses for TOI-5126 b and c are 21^{+9}_{-7} and 18^{+8}_{-6} $M_\oplus$, respectively.

The estimated RV semi-amplitudes for planets b and c are $K_b = 6.6^{+2.5}_{-2.5}$ m s^{-1} and $K_c = 3.8^{+1.5}_{-1.5}$ m s^{-1}, respectively. Measuring the masses of both planets are important to determine if they are formed with large protoplanetary cores and therefore a large gaseous envelope (Lee & Chiang) or inflated atmosphere due to tidal heating (Millholland, Petigura & Batygin 2020). TOI-5126's high-rotational velocity makes RV measurements difficult, but with the next generation of instruments such as MAROON-X (Seifahrt et al. 2018), along with innovative methods to correct for stellar variability, mass constraints of both planets are not ruled out. The rapid rotation of TOI-5126 does however enable follow-up studies into the spin-orbit alignment of the system with the Rossiter–McLaughlin effect (R–M, McLaughlin 1924; Rossiter 1924). TOI-5126 b has a predicted R–M semi-amplitude $K_b = 11.70^{+0.41}_{-0.45}$ m s^{-1}, and planet c $K_c = 7.52^{+0.43}_{-0.41}$ m s^{-1}.

The planets in the TOI-5126 system present an ideal opportunity to better understand the atmospheric composition difference between a hot super-Neptune and a warm Neptune. TOI-5126 b still likely retains a significant H/He atmosphere due to its inflated radius.

TOI-5126 is relatively bright, with a *J* band magnitude of 9.04. The inner planet TOI-5126 b has an equilibrium temperature of ($T_{eq} = 1442^{+46}_{-40}$ K), and should host a relatively clear atmosphere. To test its suitability for follow-up, we followed the transmission spectroscopy metric (TSM; Kempton et al. 2018) and find that TOI-5126 b has a TSM of 84^{+53}_{-25}. Given the potential of TOI-5126 c to also be a candidate for transmission spectroscopy (TSM = 40^{+27}_{-12}), this system enables the potential of atmospheric comparative planetology studies between a hot super-Neptune and warm Neptune. The suitability of the TOI-5126 planets for follow-up studies can be seen in comparison to the super-Neptune population in Fig. 13, where despite TOI-5126 c being a Neptune, its high-insolation flux ($S_c = 96^{+9}_{-8}$ $S_\oplus$) and predicted equilibrium temperature ($T_{eq} = 971^{+31}_{-27}$ K) make it favourable even among super-Neptunes.

To demonstrate the possibility of comparative studies, we conducted preliminary atmospheric simulations using the public soft-
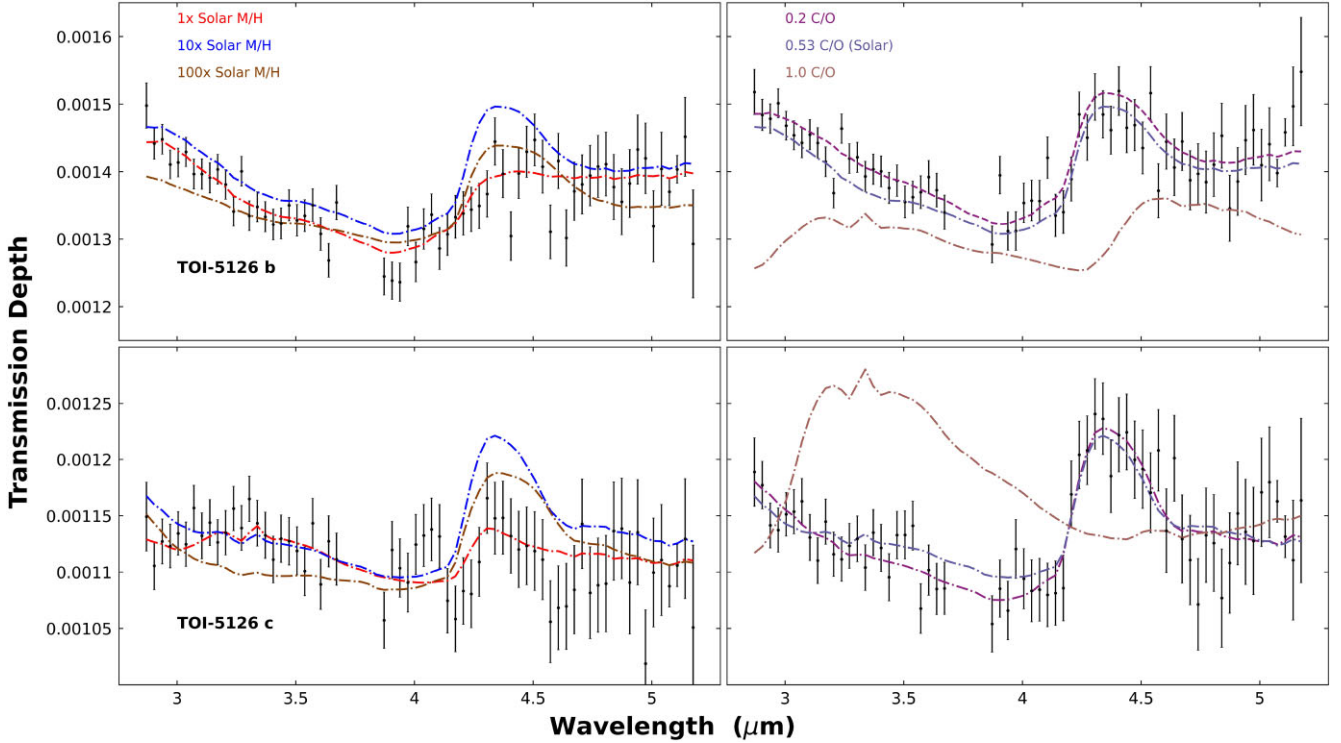
Figure 14. Simulated *JWST* Transmission Spectrums of both planets with varying metallicities and *C/O* ratios. **Left**: The red, blue, and brown lines represent the varied models of 1x, 10x, and 100x Solar M/H, respectively. **Right**: C/O simulations were based off a 10x M/H baseline. The purple, light blue, and brown lines indicate 0.2, 0.53 (Solar), and 1.0 *C/O* ratios.

ware package PETITRADTRANS (Mollière et al. 2019). As we are focused on identifying differences in the *M/H* and *C/O* ratios of the two planets, we used the NIRSpec Bright Object Time Series template with a G395H grating for our simulations. We first simulated varying *M/H*, including 1x, 10x, and 100x Solar. We also simulate the different *C/O* ratios at 0.2, 0.53 (Solar), and 1.0 *C/O* levels, in this case assuming 10x solar *M/H*. The results can be seen in Fig. 14.

The key features of the G395H grating are the CH_4 and CO_2 features in the spectra where both planets can be probed to compare formation theories. In this case, a high *C/O* ratio and metallicity would imply formation in a gas-depleted disc, while low *C/O* ratios for the planets would support other formation mechanisms. We show that differing CO_2 abundances can be discerned in both TOI-5126 b and TOI-5126 c in the M/H simulation, while TOI-5126 c appears to also have a small CH_4 feature at lower metallicities due to its lower predicted equilibrium temperature. The varying C/O models show that if TOI-5126 c has a high CH_4 abundance, its chemical signature will be apparent in the spectrum, while lower levels would as a result produce a larger CO_2 bump. The high-equilibrium temperature of TOI-5126 b diminishes the signature of the CH_4 feature at high *C/O* ratios.

ACKNOWLEDGEMENTS

We respectfully acknowledge the traditional custodians of the lands on which we conducted this research and throughout Australia. We recognize their continued cultural and spiritual connection to the land, waterways, cosmos, and community. We pay our deepest respects to all Elders, present and emerging people of the Giabal, Jarowair and Kambuwal nations, upon whose lands the MINERVA-Australis facility at Mount Kent is located.

5 DATA AVAILABILITY

All RV measurements used in our joint model analysis have been included in this paper's tables. The *TESS* data products from which we derived our light curves are publicly available online from the Mikulski Archive for Space Telescopes (MAST). Ground-based observations used in this paper are available from ExoFOP-TESS. CHEOPS data will be shared on reasonable request to the lead author.

REFERENCES

Agol E., Steffen J., Sari R., Clarkson W., 2005, MNRAS, 359, 567
Akeson R. L. et al., 2013, PASP, 125, 989
Allard F., Homeier D., Freytag B., 2012, Phil. Trans. R. Soc., 370, 2765
Armstrong D. J. et al., 2020, Nature, 583, 39
Astropy Collaboration, 2018, AJ, 156, 123
Benz W. et al., 2021, Exp. Astron., 51, 109
Borucki W. J. et al., 2010, Science, 327, 977
Brown T. M. et al., 2013, PASP, 125, 1031
Buchhave L. A. et al., 2010, ApJ, 720, 1118
Ciardi D. R., Beichman C. A., Horch E. P., Howell S. B., 2015, ApJ, 805, 16
Cincotta P. M., Simó C., 2000, A&AS, 147, 205
Cincotta P. M., Giordano C. M., Simó C., 2003, Physica D Nonlinear Phenom., 182, 151
Collins K. A., Kielkopf J. F., Stassun K. G., Hessman F. V., 2017, AJ, 153, 77
Crossfield I. J. M. et al., 2020, ApJ, 903, L7

Czesla S., Schröter S., Schneider C. P., Huber K. F., Pfeifer F., Andreasen D. T., Zechmeister M., 2019, Astrophysics Source Code Library, record(ascl:1906.010)
Dekany R. et al., 2013, ApJ, 776, 130
Eastman J. D. et al., 2019, preprint(arXiv:1907.09480)
Eisner N. L. et al., 2020, MNRAS, 494, 750
Fűrész G., Szentgyorgyi A. H., Meibom S., 2008, in Santos N. C., Pasquini L., Correia A. C. M., Romaniello M.eds, Proc. ESO/Lisbon/Aveiro Conf. Precision Spectroscopy in Astrophysics, Springer-Verlag, Berlin, p. 287
Fabricius C. et al., 2021, A&A, 649, A5
Fabrycky D. C. et al., 2012, ApJ, 750, 114
Fabrycky D. C. et al., 2014, ApJ, 790, 146
Foreman-Mackey D., Hogg D. W., Lang D., Goodman J., 2013, PASP, 125, 306
Fortney J. J., Marley M. S., Barnes J. W., 2007, ApJ, 659, 1661
Furlan E. et al., 2017, AJ, 153, 71
Gaia Collaboration, 2022, Gaia Data Release 3: Summary of the Content and Survey Properties
Giacalone S., Dressing C. D., 2020, Astrophysics Source Code Library, record, ascl:2002.004
Gillon M. et al., 2007, A&A, 472, L13
Guerrero N. M. et al., 2021, Astrophys. J. Suppl. Ser., 254, 39
Harris C. R. et al., 2020, Nature, 585, 357
Hauschildt P. H., Allard F., Ferguson J., Baron E., Alexander D. R., 1999, ApJ, 525, 871
Hayward T. L., Brandl B., Pirger B., Blacken C., Gull G. E., Schoenwald J., Houck J. R., 2001, PASP, 113, 105
Hellier C. et al., 2019, MNRAS, 488, 3067
Høg E. et al., 2000, A&A, 355, L27
Howell S. B., Everett M. E., Sherry W., Horch E., Ciardi D. R., 2011, AJ, 142, 19
Howell S. B. et al., 2014, PASP, 126, 398
Hoyer S., Guterman P., Demangeon O., Sousa S. G., Deleuil M., Meunier J. C., Benz W., 2020, A&A, 635, A24
Huang C. X. et al., 2020, Res. Notes AAS, 4, 204
Hunter J. D., 2007, Comput. Sci. Eng., 9, 90
Husser T.-O., Wende von Berg S., Dreizler S., Homeier D., Reiners A., Barman T., Hauschildt P., 2013, A&A, 553, A6
Ioannidis P., Huber K. F., Schmitt J. H. M. M., 2016, A&A, 585, A72
Jenkins J. M., Caldwell D. A., Borucki W. J., 2002, ApJ, 564, 495
Jenkins J. M. et al., 2010, in Radziwill N. M., Bridger A.eds, Proc. SPIE Conf. Ser.Vol. 7740, Software and Cyberinfrastructure for Astronomy. SPIE, Bellingham, p. 77400D
Jenkins J. M. et al., 2016, in Chiozzi G., Guzman J. C.eds, Proc. SPIE Conf. Ser.Vol. 9913, Software and Cyberinfrastructure for Astronomy IV. SPIE, Bellingham, p.99133E
Jenkins J. S. et al., 2020a, Nat. Astron., 4, 1148
Jenkins J. M., Twicken J. D., Tenenbaum P., Ting E. B., Caldwell D. A., Smith J., Rose M., Wohler B., 2020b, AAS/Division for Planetary Sciences Meeting Abstracts, p. 207.03
Jensen E., 2013, Astrophysics Source Code Library, record(ascl:1306.007)
Jin S., Mordasini C., Parmentier V., van Boekel R., Henning T., Ji J., 2014, ApJ, 795, 65
Kempton E. M.-R. et al., 2018, PASP, 130, 114401
Kipping D. M., 2013, MNRAS, 435, 2152
Kreidberg L., 2015, PASP, 127, 1161
Kurucz R. L., 1993, SYNTHE Spectrum Synthesis Programs and Line Data
Lee E. J., Chiang E., 2016a, ApJ, 817, 90
Lee E. J., Chiang E., Ormel C. W., 2014, ApJ, 797, 95
Li J., Tenenbaum P., Twicken J. D., Burke C. J., Jenkins J. M., Quintana E. V., Rowe J. F., Seader S. E., 2019, PASP, 131, 024506
Lopez E. D., 2017, MNRAS, 472, 245
Lund M. B., Ciardi D., 2020, American Astronomical Society Meeting Abstracts #235, p. 249.06
Matsakos T., Königl A., 2016, ApJ, 820, L8
Maxted P. F. L. et al., 2022, MNRAS, 514, 77
Mazeh T. et al., 2013, ApJS, 208, 16
Mazeh T., Holczer T., Faigler S., 2016, A&A, 589, A75

McCully C., Volgenau N. H., Harbeck D.-R., Lister T. A., Saunders E. S., Turner M. L., Siiverd R. J., Bowman M., 2018, in Proc. SPIE Conf. Ser. Vol. 10707, Software and Cyberinfrastructure for Astronomy V. SPIE, Bellingham, p.107070K

McLaughlin D. B., 1924, ApJ, 60, 22

Millholland S., Petigura E., Batygin K., 2020, ApJ, 897, 7

Mollière P., Wardenier J. P., van Boekel R., Henning T., Molaverdikhani K., Snellen I. A. G., 2019, A&A, 627, A67

Morris R. L., Twicken J. D., Smith J. C., Clarke B. D., Jenkins J. M., Bryson S. T., Girouard F., Klaus T. C., 2020, Kepler Data Processing Handbook: Photometric Analysis, Kepler Science Document KSCI-19081-003

Morton T. D., 2015, Astrophysics Source Code Library, record(ascl:1503.010)

Mugrauer M., Michel K.-U., 2020, Astron. Nachr., 341, 996

Mugrauer M., Michel K.-U., 2021, Astron. Nachr., 342, 840

Mugrauer M., Zander J., Michel K.-U., 2022, Astron. Nachr., 343, e24017

Otegi J. F., Bouchy F., Helled R., 2020, A&A, 634, A43

Owen J. E., Jackson A. P., 2012, MNRAS, 425, 2931

Owen J. E., Lai D., 2018, MNRAS, 479, 5012

Paredes L. A., Henry T. J., Quinn S. N., Gies D. R., Hinojosa-Goñi R., James H.-S., Jao W.-C., White R. J., 2021, AJ, 162, 176

Petigura E. A. et al., 2017, AJ, 153, 142

Quinn S. N. et al., 2012, ApJ, 745, 80

Reback J. et al., 2020, Pandas-Dev/Pandas: Pandas 1.0.3, Zenodo

Rein H., Liu S. F., 2012a, A&A, 537, A128

Rein H., Liu S. F., 2012b, A&A, 537, A128

Ricker G. R. et al., 2015, J. Astron. Telesc. Instrum. Syst., 1, 014003

Rossiter R. A., 1924, ApJ, 60, 15

Safonov B. S., Lysenko P. A., Dodin A. V., 2017, Astron. Lett., 43, 344

Sanchis-Ojeda R., Winn J. N., Holman M. J., Carter J. A., Osip D. J., Fuentes C. I., 2011, ApJ, 733, 127

Schlegel D. J., Finkbeiner D. P., Davis M., 1998, ApJ, 500, 525

Scott N. J., Howell S. B., Horch E. P., Everett M. E., 2018, PASP, 130, 1

Seifahrt A., Stürmer J., Bean J. L., Schwab C., 2018, in Evans C. J., Simard L., Takami H.eds, Proc. SPIE Conf. Ser.Vol. 10702, Ground-based and Airborne Instrumentation for Astronomy VII. SPIE, Bellingham, p. 107026D

Skrutskie M. F. et al., 2006, AJ, 131, 1163

Szabó R., Szabó G. M., Dálya G., Simon A. E., Hodosán G., Kiss L. L., 2013, A&A, 553, A17

Tamayo D. et al., 2020, Proc. Natl. Acad. Sci. USA, 117, 18194

Tokovinin A., Fischer D. A., Bonati M., Giguere M. J., Moore P., Schwab C., Spronck J. F. P., Szymkowiak A., 2013, PASP, 125, 1336

Twicken J. D., Clarke B. D., Bryson S. T., Tenenbaum P., Wu H., Jenkins J. M., Girouard F., Klaus T. C., 2010, in Software and Cyberinfrastructure for Astronomy. p. 774023

Twicken J. D. et al., 2018, PASP, 130, 064502

Vines J. I., Jenkins J. S., 2022, MNRAS, 513, 2

Virtanen P. et al., 2020, Nat. Methods, 17, 261

Wright E. L. et al., 2010, AJ, 140, 1868

Zhou G. et al., 2021, AJ, 161, 2

Ziegler C., Tokovinin A., Briceño C., Mang J., Law N., Mann A. W., 2020, AJ, 159, 19

[1] *Centre for Astrophysics, University of Southern Queensland, West St, Darling Heights, Toowoomba, Queensland 4350, Australia*

[2] *Department of Physics and Kavli Institute for Astrophysics and Space Research, Massachusetts Institute of Technology, 77 Massachusetts Ave, Cambridge, MA 02139, USA*

[3] *Sternberg Astronomical Institute, Lomonosov Moscow State University, Universitetskii prospekt 13, 119992 Moscow, Russia,*

[4] *Center for Astrophysics|Harvard & Smithsonian, 60 Garden Street, Cambridge, MA 02138, USA*

[5] *NASA Exoplanet Science Institute - Caltech/IPAC, 1200 E. California Blvd, Pasadena, CA 91125, USA*

[6] *George Mason University, 4400 University Drive, Fairfax, VA 22030, USA*

[7] *NSF's National Optical-Infrared Astronomy Research Laboratory, 950 N. Cherry Avenue, Tucson, AZ 85719, USA*

[8] *NASA Ames Research Center, Moffett Field, CA 94035, USA*

[9] *Instituto de Astrofísica de Canarias (IAC), E-38205 La Laguna, Tenerife, Spain*

[10] *Departamento de Astrofísica, Universidad de La Laguna (ULL), E-38206 La Laguna, Tenerife, Spain*

[11] *Kotizarovci Observatory, Sarsoni 90, 51216 Viskovo, Croatia*

[12] *Department of Earth, Atmospheric, and Planetary Sciences, Massachusetts Institute of Technology, Cambridge, MA 02139, USA*

[13] *Department of Aeronautics and Astronautics, Massachusetts Institute of Technology, Cambridge, MA 02139, USA*

[14] *Department of Astrophysical Sciences, Princeton University, Princeton, NJ 08544, USA*

[15] *Department of Astronomy, California Institute of Technology, MC 249-17, Pasadena, CA 91125, USA*

[16] *Department of Physics and Astronomy, University of New Mexico, 210 Yale Blvd NE, Albuquerque, NM 87106, USA*

[17] *Center for Computational Astrophysics, Flatiron Institute, 162 5th Ave New York, NY 10010, USA*

This paper has been typeset from a TEX/LATEX file prepared by the author.